Electronic Supplementary Material (ESI) for Energy & Environmental Science
This journal is © The Royal Society of Chemistry 2013

# SUPPLEMENTARY MATERIALS

## S1. SOLAR CELL FABRICATION

The details of cell fabrication have been reported in earlier publications (see respective references). We have provided a brief summary of the processes below, for quick reference.

### AMORPHOUS SILICON P-I-N CELLS [1]

The cells were prepared using plasma enhanced chemical vapor deposition (PECVD) of a-Si:H, on Fluorinated Tin Oxide (FTO) coated glass, which acts as the p-contact. The p/i/n layer thicknesses are 10nm/250nm/20nm respectively. Finally, Aluminum doped ZnO (AZO) and Ag were deposited as the n-contact. The cell area was $0.5cm^2$. A schematic of the cell structure is shown in the inset of Fig. 3a.

### BULK HETEROJUNCTION (BHJ) ORGANIC SOLAR CELLS [2]

For the BHJ OPV cells first the hole conducting poly(3,4-ethylenedioxythiophene) poly(styrenesulfonate) (PEDOT:PSS) layer was spin-casted on Indium doped Tin Oxide (ITO) coated glass substrate. This was followed by spin-casting of a dicholorobenzene (DCB) solution of poly(3-hexylthiophene) (P3HT) and the fullerene derivative [6,6]-phenyl-$C_{61}$ butyric acid methyl ester (PCBM), and thermal annealing. Finally LiF and Al were evaporated to form the cathode layers. The cell area was $0.06cm^2$. A schematic of the cell structure is given in the inset of Fig. 3b.

### CIGS CELLS [3]

For CIGS cells, first $Cu_2(In_{0.7},Ga_{0.3})S_2$ were synthesized in a solution of metal-acetylacetoacetate precursors. After dispersing the particles in hexanethiol, they were cast into thin films using doctor blade technique, on Mo coated glass. This was followed by KCN etch, and dip into NaCl solution. The films were then annealed in Se vapor, resulting in formation of polycrystalline $Cu_2(In_{0.7},Ga_{0.3})(S_{1-y},Se_y)$ films. Finally, the CdS emitter was deposited using chemical bath deposition, and the device was finished by sputtering of ZnO and ITO layers. The device area was $0.47cm^2$. The schematic of cell structure is given in the inset of Fig. 3c.

### CDTE CELLS [4]

The CdTe cells were prepared on fluorinated tin oxide coated soda lime glass. First, the n-CdS layer was deposited using chemical bath deposition, followed by closed space sublimation of CdTe thin film. The device was completed by sputtering the Ni/C back contact layer. The device area was $0.7cm^2$. The schematic of cell structure is given in inset of Fig. 3d.

## S2. SPACE-CHARGE-LIMITED SHUNT CURRENT

In our earlier publications [1], [5], we had developed and validated a space-charge-limited (SCL) model for shunt current in TFPV cells. Here, we provide a brief summary of this work, and reproduce some figures, to provide context to the shunt statistics work. Shunt current in TFPV cells (a-Si:H, BHJ OPV, and CIGS), exhibits certain universal voltage and temperature dependencies, which differentiate it from exponential diode current. These observed features can be summarized as –

This journal is © The Royal Society of Chemistry 2013

- Symmetric with respect to voltage about $V = 0$ point i.e. $I_{SH}(-V) \approx -I_{SH}(V)$.
- Non-ohmic power-law voltage dependence i.e. $I_{SH} \propto V^{\beta}$, where $\beta \sim 2-3$.
- Weak temperature dependence i.e. $I_{SH} \propto T^{1-2}$.

These observed features were consistent across the three thin film solar cells considered in the work. We were able to explain these characteristics of the shunt current using a *phenomenological* SCL model of shunt conduction, which explained the dark IV of TFPV cells using a parallel combination of an intrinsic exponential diode current in parallel with a parasitic SCL shunt current. As discussed in the paper, the SCL model is able to account for all the above observed terminal characteristics of $I_{SH}$ and reproduce the voltage and temperature dependencies of dark IV. This can also be seen from the generalized expression of SCL current for materials with shallow traps

$$I_{SCL} = A\epsilon\mu_c(\gamma)\frac{V^{\gamma+1}}{L^{2\gamma+1}}.$$

Here, $\epsilon$ is the material permittivity, $\mu_c$ is the effective carrier mobility, $\gamma$ is a material parameter determined by the trap distribution inside the material, A is the cross sectional area, and $L$ is the layer thickness. From eq. (S1) we can readily see the symmetric power-law voltage dependence, and the carrier mobility being the only temperature dependent term, explains the weak temperature dependence. Note that this is a phenomenological model, which does not require any assumptions regarding the nature of shunt paths.

The insights from the model, however, have helped us in exploring the physical origin of shunt paths. We know from the SCL model of shunt conduction that an SCL shunt path requires a symmetric Metal/Semiconductor/Metal type structure for ensuring single carrier transport [6] (see Fig. S1). Moreover, parasitic shunt current had been linked to localized defects on the solar cell surface. A variety of studies, using various techniques [7–10], on very different technologies have confirmed this local nature of shunt defects [11–14]. Combining these two insights, we proposed that parasitic shunts are formed due to local non-uniformities, which can lead to destruction of the junction locally and formation of a symmetric MSM type path. These non-uniformities can arise from a variety of sources, including but not limited to metal incorporation from contact layers [15], non-uniform deposition of thin emitter layers [16], surface roughness in absorbers or substrates [17], and pinholes in the inter-layers [18].

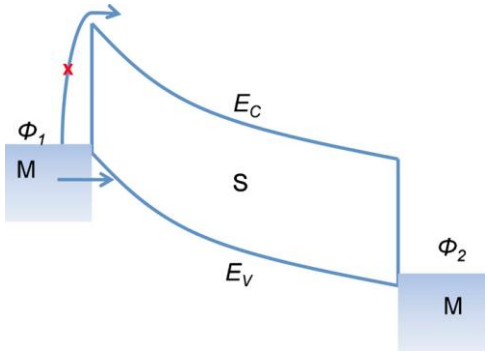


*Figure S1. Schematic and band diagram of a MSM structure, showing SCL transport. The metal work functions* $\phi_1 \approx \phi_2$ *ensure that holes are injected preferentially into the semiconductor.*

In case of amorphous silicon p-i-n cells, we identified metal incorporation from the top contact as the most likely cause, which leads to the formation of a localized p-i-p shunt path (only hole transport) in parallel to the p-i-n diode structure of the solar cell, shown schematically in Fig. S2a. The metal incorporation hypothesis for a-Si:H is supported by high Al mobility in a-Si:H [19], and metastable switching if shunt paths with applied bias [20], amongst other evidences. We then used full 2D TCAD simulations to demonstrate that this structure can actually

This journal is © The Royal Society of Chemistry 2013

reproduce the observed features of shunt current in a-Si:H cells, as shown in Fig. S2b. Using this simulation approach, we were able to reproduce the voltage and temperature dependencies of dark current in a-Si:H, BHJ OPV, and CIGS cells, using physical parameters, and full TCAD device simulations (see Fig. S3).

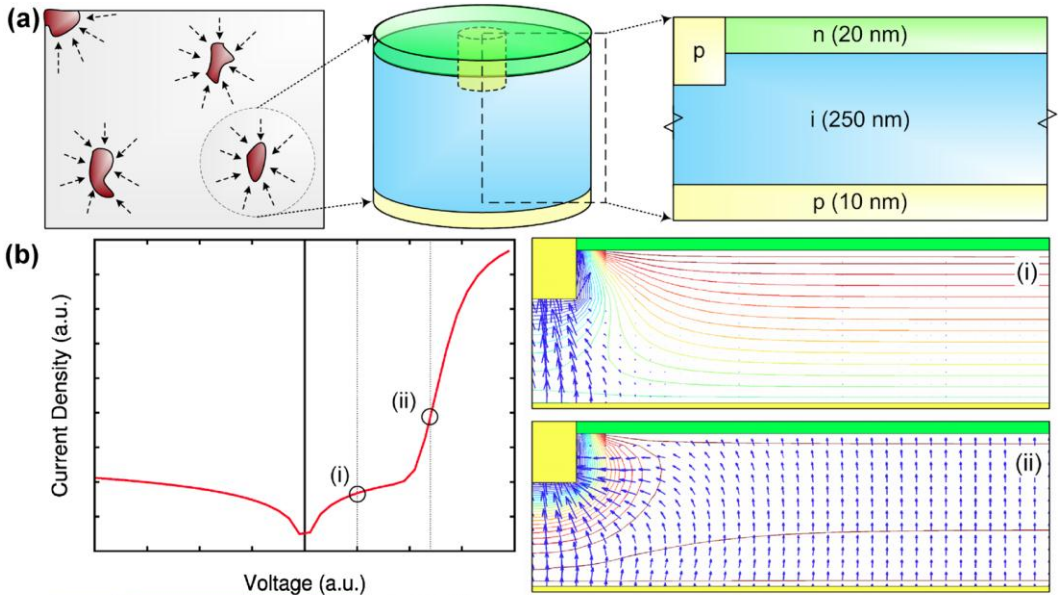


*Figure S2. (a) Schematics showing the top view of a solar cell surface with localized shunts. A cylinder is drawn around the shunt region (shown for an a-Si:H p-i-n solar cell) with the shunt formed due to Al incursion. A 2D simulation structure (formed by taking a vertical cut), simulated using cylindrical coordinates, with the p-i-p region in the middle forming the shunt. (b) The dark IV obtained from the 2D simulation of the structure in part (a), reproduces the features of shunt conduction. The quiver (current density) and contour plots (potential), corresponding to the shunt dominated regime (green vertical line denoted by (i)), and the diode dominated regime (blue vertical line denoted by (ii)), showing the localization of dark current at low biases, resulting in a shunt-dominated region.*

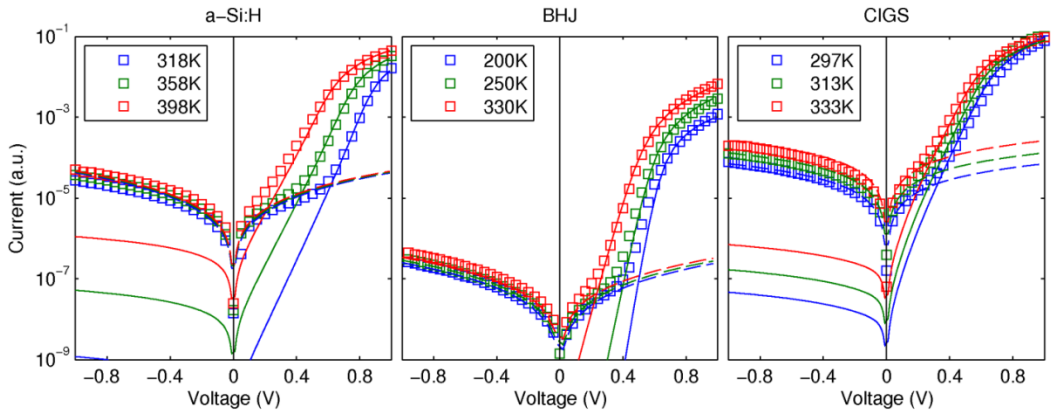


*Figure S3. Simulations of the 1D ideal solar cell structures (solid lines) at three different temperatures along with the corresponding shunt structures (dashed lines), showing good agreement with experiment for all PV technologies (symbols). The combination of these two current components explains the entire dark IV response at the indicated temperatures.*

This journal is © The Royal Society of Chemistry 2013

## S3. SPICE SIMULATION OF TFPV MODULES

In order to illustrate the importance of shunt statistics on module performance and variability, we use 2D equivalent circuit network simulations with SPICE. The approach allows us to simulate typical TFPV modules ($L_{module} \times W_{module} \sim 1m^2$, with $N_{series} \sim 100$ cells in series), by dividing each thin rectangular cell into $N_{parallel}$ number of sub-cells. These sub-cells are connected in series and parallel using appropriate contact sheet resistances to form the 2D network circuit representation of the module. This process is shown schematically in Fig. S4a, and has been used in the past for module level simulations in various monolithic TFPV technologies [21–23].

Note that this framework simulates the more common monolithically manufactured modules for these four technologies. In some cases, however, a roll-to-roll manufacturing on flexible substrates is used; which allows individual cells to be cut from the larger role [24], [25]. These cells can then be tested and sorted, and the modules are then formed separately by taking cells from a particular bin. While this may help in reducing the cell mismatch at module level, we must remember that the number of cells in each bin will still be determined by the log-normal shunt statistics, and will in turn determine the process yield of these technologies. Also, just like multi-crystalline Si cells, these roll-to-roll process cells will have certain amount of mismatch even after binning. These residual mismatches, although smaller than monolithic case, will lead to certain module efficiency loss. This can be analyzed using established 1D simulation method for crystalline modules[26]. In this work, we focus on the more common monolithic TFPV modules, which require a full 2D circuit simulation for analysis of variability effects.

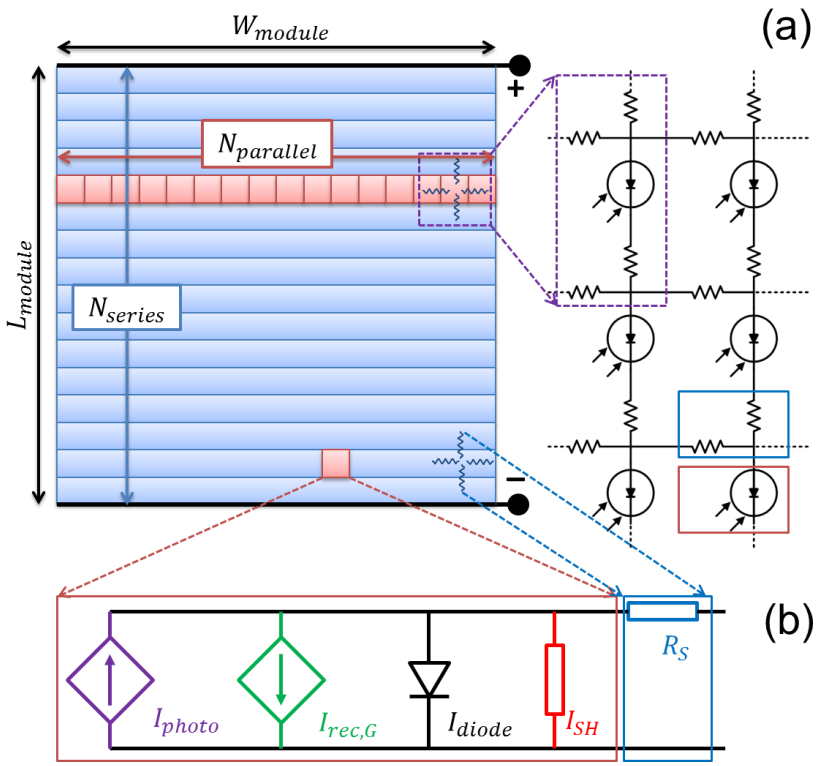


*Figure S4. (a) Schematic showing the circuit representation of a TFPV module with rectangular series connected cells, by subdividing each cell into sub-cells, connected in series and parallel to form a 2D network circuit shown on the right. (b) Sub-cell equivalent circuit used in this simulation showing the photo and dark current fluxes with relevant voltage dependencies.*

This journal is © The Royal Society of Chemistry 2013

## S3.1 SUB-CELL EQUIVALENT CIRCUIT

For typical module dimensions, the sub-cells are $\sim 1cm^2$ in size, and we use physics based equivalent circuit for TFPV cells to model the device characteristics (see Fig. S4b). The equivalent circuit takes into account the intrinsic current fluxes, namely voltage dependent photocurrent ($I_{photo}$) [27], generation enhanced recombination ($I_{rec,G}$) [28], and the dark diode current $I_{diode}$ [29]; as well as parasitic non-Ohmic shunt current $I_{SH}$ [5]. The sheet resistance values are used to calculate the $R_S$ values for series and parallel connections. Note that the equivalent circuit in Fig. S4b can be derived analytically for a-Si:H cells [30], but it can also be used effectively as a semi-empirical equivalent circuit for other TFPV technologies [31].

We use the equivalent circuit shown in Fig. S4b to assess the effect of $I_{SH0}$ on sub-cell efficiency. We first fit the reported record cell efficiency $\eta_{max}$ [32] by tweaking the intrinsic parameters (i.e., $I_{photo}$, $I_{rec,G}$, and $I_{diode}$) of the equivalent circuit shown in Fig. S4b. Table S1 shows the record (or near record) efficiencies, and performance parameters, reported for different technologies along with sources. We fit the equivalent circuit in Fig. S4b to these parameters for each technology to obtain the respective $\eta_{max}$. We then simulate this sub-cell circuit in SPICE with $I_{SH0}$ values varying over many orders of magnitude to obtain the relation between sub-cell efficiency $\eta$ and $I_{SH0}$, as shown in Fig. 5a for a-Si:H. The relation between shunt dependent sub-cell efficiency ($\eta(I_{SH0})$) with the statistics of shunt formation in a particular technology, determines the overall module efficiency for that technology.

*Table S1. Highest reported cell performance numbers for different technologies from different manufacturers. The exact record efficiencies for each might be slightly different.*

| | Sub-cell parameters | | | |
|---|---|---|---|---|
| | $J_{SC}$ $(mA/cm^2)$ | $V_{OC}$ $(V)$ | $FF$ $(\%)$ | $\eta_{sub}$ $(\%)$ |
| **a-Si:H (Moserbaer)**[33] | 15.87 | 0.89 | 68.3 | 9.6 |
| **OPV (Konarka)** [34] | 16.4 | 0.82 | 70 | 8.3 |
| **CIGS (Solar Frontier)**[35] | 33.0 | 0.688 | 76.7 | 17.4 |
| **CdTe (First Solar)** [32] | 27.1 | 0.827 | 76.6 | 17.2 |

## S3.2 EFFECT OF SHUNTED SUB-CELLS

In order to illustrate the effect of log-normal shunt statistics on module efficiency, we simulate a $10 \times 10cm^2$ TFPV sub-module, with 10 cells in series. Each series connected cell is $1 \times 10cm^2$ (horizontal rectangles in Fig. S5) is subdivided into $1 \times 1cm^2$ sub-cells as shown in Fig. S4a. We use typical a-Si:H solar cell, with highest efficiency of 9.8% [36], as an example to demonstrate the principle. We assign each sub-cell a different $I_{SH0}$ value, obtained from the measured log-normal distribution (see Fig. S5a), keeping all other parameters identical. In order to understand the effect of shunt variability in this series connected module let us focus on cell number 9 in the sub-module shown in Fig. S5a. We can see that this cell has one shunted sub-cell in the middle (circled) and the rest of them would be near $\eta_{max}$. This is expected from the efficiency vs. $I_{SH0}$ curve in Fig. 5a, which predicts only few shunted low efficiency cells, while rest are close to $\eta_{max}$.

We can evaluate the impact of these distributed shunt defects by simulating this 2D circuit, and analyzing the sub-cell behavior at the maximum power point (MPP) of the sub-module. Fig. S5b shows the operating voltage of each sub-cell, when the module is operating at its MPP voltage. Note that for cells with small or no shunting (cell no. 2 e.g.), all sub-cells operate at their respective MPP of $\sim 0.8V$. In cell no. 9 with one shunted sub-cell, however, the bias of the entire row of sub-cells is modified to $\sim 0.3 - 0.4V$ range (highlighted). Thus, we can see that a single

This journal is © The Royal Society of Chemistry 2013

heavily shunted sub-cell disturbs the operation of up to 10 of its neighbors, and biases them significantly away from their MPP voltage.

In addition, when we plot the power output of each sub-cell (Fig. S5c), we can see that the shunted sub-cell is actually *consuming* power (negative sign), when the good cells are producing power ($\sim 10mW$ per sub-cell). This is power being dissipated in the shunted sub-cell is supplied by the power output of its neighboring sub-cells (circled in Fig. S5c). This situation arises from the requirement of current continuity enforced by series connection of cells, and the influence of contact sheet resistance connecting these different sub-cells. Thus, we can see that the shunted sub-cells have a twofold effect on the module output power, arising from the interconnection related issues. As a result, while these heavily shunted cells from the tail of this distribution are few in number, they have a disproportionately large impact on the overall sub-module efficiency. This discussion highlights the consequences this 'heavy tailed' shunt distribution with regards to module efficiency and variability.

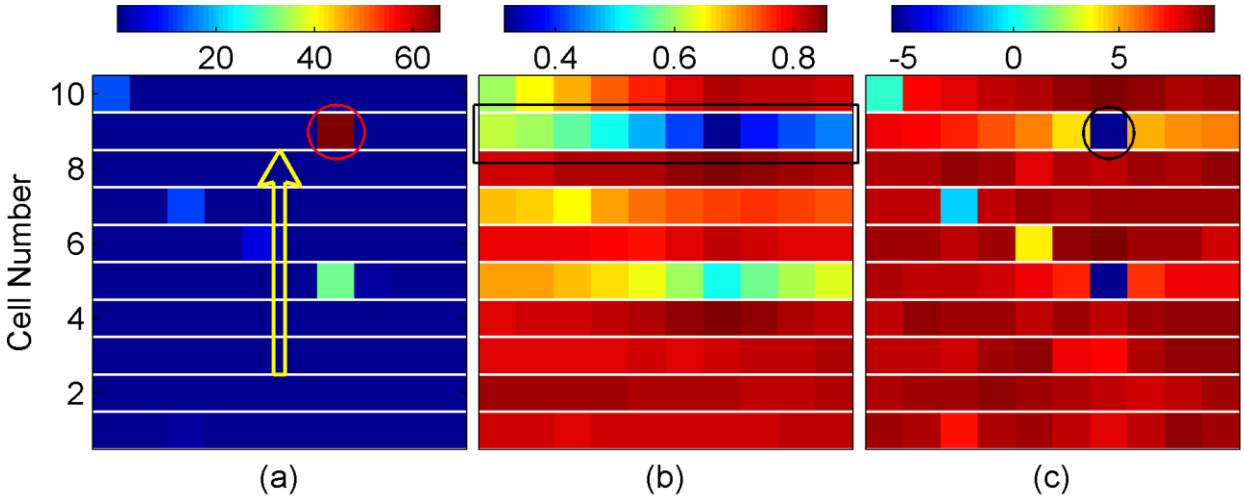


*Figure S5. (a) Color plot of $I_{SH0}$ values (color bar in a.u.) across a series connected sub-module (arrow shows direction of current flow), with each sub-cell (squares) assigned different $I_{SH0}$ value obtained from log-normal distribution. (b) Color plot of sub-cell operating voltage (color bar in V), when the sub-modules is biased at its MPP voltage, showing that the shunted sub-cells distort the operating voltage of its good neighboring sub-cells. (c) Color plot of power output (positive sign) across the sub-module (color bar in mW), showing the shunted sub-cells consuming (negative sign) the power output of its neighboring regions.*

## S3.3 Monte-Carlo simulation of module efficiency

We can also use the module simulation technique to assess the impact of shunt statistics on module performance and variability. For each technology, we use the equivalent circuit in Fig. S4b fitted to the respective $\eta_{max}$, as the sub-cell equivalent circuit. We then simulate the module IV curve multiple times, assigning different $I_{SH0}$ values to the sub-cells according to the measured log-normal distribution (from Fig. 3). We assume all other parameters to be identical across the sub-cells. The module dimensions and structures are obtained from manufacturer data sheets, and the sheet resistance values for TCO and metal contacts are assumed to be $10\Omega/sq$ and $0.5\Omega/sq$ [33], respectively. A summary of module dimensions and parameters, along with sources, is provided in table S2.

In this way, we can obtain the distribution of module efficiency for a given distribution of $I_{SH0}$, for all four technologies. The result from this simulation for a-Si:H cells is shown in Fig. 6a, comparing the record cell efficiency, with the best module efficiency (without any shunts), and the distribution of module efficiency in

This journal is © The Royal Society of Chemistry 2013

presence of log-normal shunt distribution [37]. By repeating this analysis for all four TFPV technologies, we can reproduce the gap between cell and module efficiencies, to a reasonably reasonable degree, as shown in Fig. 6b.

*Table S2. Module parameters used for the Monte-Carlo simulation of module efficiency, using the measured log-normal $I_{SH0}$ distribution for the four technologies.*

| | Module parameters | | | | |
|---|---|---|---|---|---|
| | $L_{module}$ $(cm)$ | $W_{module}$ $(cm)$ | $N_{series}$ | $R_{sq}^{top}, R_{sq}^{bot}$ $(\Omega/square)$ | $\langle\eta_{module}\rangle$ $(\%)$ |
| **a-Si:H (Moserbaer)** [36] | 110 | 130 | 104 | 10, 0.5 | 7.6 |
| **OPV (Konarka)*** [38] | 40 | 20 | 40 | 10, 10 # | 3.4 |
| **CIGS (Solar Frontier)** [39] | 150 | 115 | 90 | 10, 0.5 | 12.2 |
| **CdTe (First Solar)** [40] | 116 | 56 | 116 | 10, 0.5 | 12.5 |

* sub-module dimensions (modules consist of 5 or more sub-modules connected externally)
# both contacts are TCO

Note that this is only a sample simulation, and the sub-cell efficiency data, module parameters, and shunt statistics data are collected from different sources. Therefore, the gap between cell and module efficiency obtained from this simulation is only indicative. A precise assessment of impact of shunt statistics will require a controlled and calibrated data on physical parameters, as well as statistical distribution, from the same process. The purpose of this simulation is to demonstrate that it is possible to incorporate statistical variability into module simulations, and obtain useful results from the analysis. The calculation also reinforces the importance of the universality in shunt statistics, by showing that although the simulation is not exactly calibrated to the data; we are still able to obtain reasonable results just by accounting for the log-normal nature of shunt distribution.

## REFERENCES

[1] S. Dongaonkar, K. Y, D. Wang, M. Frei, S. Mahapatra, and M. A. Alam, "On the Nature of Shunt Leakage in Amorphous Silicon p-i-n Solar Cells," *IEEE Electron Device Letters*, vol. 31, no. 11, pp. 1266–1268, Nov. 2010.

[2] M. D. Irwin, D. B. Buchholz, a. W. Hains, R. P. H. Chang, and T. J. Marks, "p-Type semiconducting nickel oxide as an efficiency-enhancing anode interfacial layer in polymer bulk-heterojunction solar cells," *Proceedings of the National Academy of Sciences*, vol. 105, no. 8, pp. 2783–2787, Feb. 2008.

[3] Q. Guo, G. M. Ford, H. W. Hillhouse, and R. Agrawal, "Sulfide nanocrystal inks for dense Cu(In1-xGa(x))(S1-ySe(y))2 absorber films and their photovoltaic performance.," *Nano letters*, vol. 9, no. 8, pp. 3060–3065, Aug. 2009.

[4] D. H. Rose, F. S. Hasoon, R. G. Dhere, D. S. Albin, R. M. Ribelin, X. S. Li, Y. Mahathongdy, T. A. Gessert, and P. Sheldon, "Fabrication procedures and process sensitivities for CdS/CdTe solar cells," *Progress in Photovoltaics: Research and Applications*, vol. 7, no. 5, pp. 331–340, Sep. 1999.

[5] S. Dongaonkar, J. D. Servaites, G. M. Ford, S. Loser, J. Moore, R. M. Gelfand, H. Mohseni, H. W. Hillhouse, R. Agrawal, M. A. Ratner, T. J. Marks, M. S. Lundstrom, and M. A. Alam, "Universality of non-Ohmic shunt leakage in thin-film solar cells," *Journal of Applied Physics*, vol. 108, no. 12, p. 124509, 2010.

This journal is © The Royal Society of Chemistry 2013

[6] A. Rose, “Space-Charge-Limited Currents in Solids,” *Physical Review*, vol. 97, no. 6, pp. 1538–1544, Mar. 1955.

[7] H. Straube, J.-M. Wagner, J. Schneider, and O. Breitenstein, “Quantitative evaluation of loss mechanisms in thin film solar cells using lock-in thermography,” *Journal of Applied Physics*, vol. 110, no. 8, p. 084513, Oct. 2011.

[8] T. Ott, F. R. Runai, F. Schwäble, and T. Walter, “2D network simulation and luminescence characterization of Cu(In,Ga)Se2 thin film modules,” *Progress in Photovoltaics: Research and Applications*, p. n/a–n/a, Mar. 2012.

[9] A. Helbig, T. Kirchartz, R. Schaeffler, J. H. Werner, and U. Rau, “Quantitative electroluminescence analysis of resistive losses in Cu(In, Ga)Se2 thin-film modules,” *Solar Energy Materials and Solar Cells*, vol. 94, no. 6, pp. 979–984, Jun. 2010.

[10] I. Tarasov, S. Ostapenko, and J. P. Kalejs, “Defect monitoring using scanning photoluminescence spectroscopy in multicrystalline silicon solar cell,” *Conference Record of the Twenty-Eighth IEEE Photovoltaic Specialists Conference - 2000 (Cat. No.00CH37036)*, vol. 840, pp. 112–115, 2000.

[11] O. Breitenstein, J. P. Rakotoniaina, M. H. Al Rifai, and M. Werner, “Shunt types in crystalline silicon solar cells,” *Progress in Photovoltaics: Research and Applications*, vol. 12, no. 7, pp. 529–538, Nov. 2004.

[12] A. Virtuani, E. Lotter, M. Powalla, U. Rau, J. H. Werner, and M. Acciarri, “Influence of Cu content on electronic transport and shunting behavior of Cu(In,Ga)Se[sub 2] solar cells,” *Journal of Applied Physics*, vol. 99, no. 1, p. 014906, 2006.

[13] T. J. McMahon and M. S. Bennett, “Metastable shunt paths in a-Si solar cells,” *Solar Energy Materials and Solar Cells*, vol. 41–42, pp. 465–473, Jun. 1996.

[14] T. J. McMahon, T. J. Berniard, and D. S. Albin, “Nonlinear shunt paths in thin-film CdTe solar cells,” *Journal of Applied Physics*, vol. 97, no. 5, p. 054503, 2005.

[15] J. Won Seo, S. J. Baik, S. J. Kang, Y. H. Hong, J.-H. Yang, L. Fang, and K. S. Lim, “Evidence of Al induced conducting filament formation in Al/amorphous silicon/Al resistive switching memory device,” *Applied Physics Letters*, vol. 96, no. 5, pp. 053504–3, 2009.

[16] J. D. Major and K. Durose, “Study of buried junction and uniformity effects in CdTe/CdS solar cells using a combined OBIC and EQE apparatus,” *Thin Solid Films*, vol. 517, no. 7, pp. 2419–2422, Feb. 2009.

[17] M. D. Irwin, J. Liu, B. J. Leever, J. D. Servaites, M. C. Hersam, M. F. Durstock, and T. J. Marks, “Consequences of Anode Interfacial Layer Deletion. HCl-Treated ITO in P3HT:PCBM-Based Bulk-Heterojunction Organic Photovoltaic Devices,” *Langmuir*, vol. 26, no. 4, pp. 2584–2591, Feb. 2009.

This journal is © The Royal Society of Chemistry 2013

[18] O. Kunz, J. Wong, J. Janssens, J. Bauer, O. Breitenstein, and A. Aberle, "Shunting problems due to sub-micron pinholes in evaporated solid-phase crystallised poly-Si thin-film solar cells on glass," *Progress in Photovoltaics: Research and Applications*, vol. 17, no. 1, pp. 35–46, Jan. 2009.

[19] M. Jafar and D. Haneman, "Switching in amorphous-silicon devices," *Physical Review B*, vol. 49, no. 19. pp. 13611–13615, May-1994.

[20] S. Dongaonkar, K. Y., S. Mahapatra, and M. A. Alam, "Physics and Statistics of Non-Ohmic Shunt Conduction and Metastability in Amorphous Silicon p–i–n Solar Cells," *IEEE Journal of Photovoltaics*, vol. 1, no. 2, pp. 111–117, Oct. 2011.

[21] G. T. Koishiyev and J. R. Sites, "Impact of sheet resistance on 2-D modeling of thin-film solar cells," *Solar Energy Materials and Solar Cells*, vol. 93, no. 3, pp. 350–354, 2009.

[22] J. Johansson, "Modelling and Optimization of CIGS Solar Cell Modules," Lunds University, 2008.

[23] B. E. Pieters, "Spatial Modeling of Thin-Film Solar Modules Using the Network Simulation Method and SPICE," *IEEE Journal of Photovoltaics*, vol. 1, no. 1, pp. 93–98, Jul. 2011.

[24] "Thin Film - Miasole," 2012. [Online]. Available: http://www.miasole.com/thin-film.

[25] "nanosolar - Technology Overview," 2012. [Online]. Available: http://www.nanosolar.com/technology/technology-overview/.

[26] J. W. Bishop, "Computer simulation of the effects of electrical mismatches in photovoltaic cell interconnection circuits," *Solar Cells*, vol. 25, pp. 73–89, 1988.

[27] R. Sokel and R. Hughes, "Numerical analysis of transient photoconductivity in insulators," *Journal of Applied Physics*, vol. 53, no. 11, p. 7414, 1982.

[28] J. Merten, J. M. Asensi, C. Voz, A. V. Shah, R. Platz, and J. Andreu, "Improved equivalent circuit and analytical model for amorphous silicon solar cells and modules," *IEEE Transactions on Electron Devices*, vol. 45, no. 2, pp. 423–429, 1998.

[29] F. A. Rubinelli, J. K. Arch, and S. J. Fonash, "Effect of contact barrier heights on a-Si:H p-i-n detector and solar-cell performance," *Journal of Applied Physics*, vol. 72, no. 4, p. 1621, 1992.

[30] S. Dongaonkar, C. Deline, and M. A. Alam, "Performance and Reliability Implications of Two Dimensional Shading in Monolithic Thin Film Photovoltaic Modules," *(Under Review)*.

[31] S. Hegedus, D. Desai, and C. Thompson, "Voltage dependent photocurrent collection in CdTe/CdS solar cells," *Progress in Photovoltaics: Research and Applications*, vol. 15, no. 7, pp. 587–602, Nov. 2007.

[32] M. A. Green, K. Emery, Y. Hishikawa, W. Warta, and E. D. Dunlop, "Solar cell efficiency tables (version 40)," *Progress in Photovoltaics: Research and Applications*, vol. 20, no. 5, pp. 606–614, Aug. 2012.

This journal is © The Royal Society of Chemistry 2013

[33] W. Hoffmann, “Technologieentwicklung für Dünnschichtund kristalline Silizium-basierte Photovoltaik,” 2008. [Online]. Available: http://www.cismst.org/fileadmin/user_upload/news/Hoffmann_AppliedMaterials.pdf.

[34] M. A. Green, K. Emery, Y. Hishikawa, and W. Warta, “Solar cell efficiency tables (version 37),” *Progress in Photovoltaics: Research and Applications*, vol. 19, no. 1, pp. 84–92, Jan. 2011.

[35] D. L. Edelman, “Solar Frontier Sets New Efficiency World Record,” 2012. [Online]. Available: http://www.solar-frontier.com/eng/news/2012/C002980.html.

[36] “Moserbaer Solar, Power Series QS: Amorphous Silicon Thin Film Modules.” [Online]. Available: http://www.moserbaersolar.com/resources/thinfilms-english QS-latest.pdf. [Accessed: 08-Jan-2012].

[37] S. Dongaonkar and M. A. Alam, “End-to-End Modeling for Variability and Reliability Analysis of Thin Film PV,” in *2012 IEEE International Reliability Physics Symposium (IRPS 2012)*, 2012, pp. 4A.4.1 – 4A.4.6.

[38] “Konarka Tech Sheets & Brochures - Konarka Technologies,” 2012. [Online]. Available: http://www.konarka.com/index.php/company/tech-sheets-and-brochures/. [Accessed: 26-Apr-2012].

[39] “Solar Frontier SF140-160-S module series.” [Online]. Available: http://www.solar-frontier.com/eng/products/modules/S002210.html. [Accessed: 08-Jan-2013].

[40] “First Solar FS Series 3 PV Module Datasheet.” [Online]. Available: http://www.firstsolar.com/Company-Documentation. [Accessed: 08-Jan-2013].